ELECTROMAGNETIC METAL FORMING

Ruben Otin, Roger Mendez and Oscar Fruitos

CIMNE - International Center For Numerical Methods in Engineering
Parque Mediterráneo de la Tecnología (PMT)
E-08860 Castelldefels (Barcelona, Spain)
tel.: +34 93 413 41 79, e-mail: rotin@cimne.upc.edu

Barcelona, July 2011

Contents

Chapter 1

Electromagnetic metal forming

This report presents a numerical model for computing the Lorentz force that drives an electromagnetic forming process. This model is also able to estimate the optimum capacitance at which it is attained the maximum workpiece deformation. The input data required are the geometry and material properties of the system coil-workpiece and the electrical parameters of the capacitor bank. The output data are the optimum capacitance, the current flowing trough the coil and the Lorentz force acting on the workpiece. The main advantage of our approach is that it provides an explicit relation between the capacitance of the capacitor bank and the frequency of the discharge, which is a key parameter in the design of an electromagnetic forming system. The model is applied to different forming processes and the results compared with theoretical predictions and measurements of other authors. The work is part of the project SICEM (SImulación multifísica para el diseño de Conformado ElectroMagnético), Spanish MEC National R+D Plan 2004-2007, ref.: DPI2006-15677-C02-01.

1.1 Introduction

Electromagnetic forming (EMF) is a high velocity forming technique that uses electromagnetic forces to shape metallic workpieces. The process starts when a capacitor bank is discharged through a coil. The transient electric current which flows through the coil generates a time-varying magnetic field around it. By Faraday's law of induction, the time-varying magnetic field induces electric currents in any nearby conductive material. According to Lenz's law, these induced currents flow in the opposite direction to the primary currents in the coil. Then, by Ampere's force law, a repulsive force arises between the coil and the conductive material. If this repulsive force is strong enough to stress the workpiece beyond its yield point then it can shape it with the help of a die or a mandrel.

Although low-conductive, non-symmetrical, small diameter or heavy gauge workpieces can not be suitable for EMF, this technique present several advantages. For example: no tool marks are produced on the surfaces of the workpieces, no lubricant is required, improved formability, less wrinkling, controlled springback, reduced number of operations and lower energy cost. In order to successfully design sophisticated EMF systems and control their performance, it is necessary to

advance in the development of theoretical and numerical models of the EMF process. This is the objective of the present work. More specifically, we focus our attention on the numerical analysis of the electromagnetic part of the EMF process. For a review on the state-of-the-art of EMF see [5, 7, 14] or the introductory chapters in [16, 19, 4, 20], where it is given a general overview about the EMF process and also abundant bibliography.

In this report we present a method to compute numerically the Lorentz force that drives an EMF process. We also estimate the optimum frequency and capacitance at which it is attained the maximum workpiece deformation for a given initial energy and a given set of coil and workpiece. The input data required are the geometry and material properties of the system coil-workpiece and the electrical parameters of the capacitor bank. With these data and the time-harmonic Maxwell's equations we are able to calculate the optimum capacitance, the current flowing trough the coil and the electromagnetic forces acting on the workpiece. The main advantage of this method is that it provides an explicit relation between the capacitance of the capacitor bank and the frequency of the discharge which, as it is shown in [10, 28, 9], is a key parameter in the design of an EMF system. Also, our frequency domain approach is computationally efficient and it offers an alternative to the more extended time domain methods.

In section 1.2 we summarize the coupling strategies which connect the electromagnetic equations with the other physical phenomena involved in an EMF process.

In section 1.3 we explain in detail the electromagnetic model employed in this work. We show the general formulas and the assumptions we made to compute the intensity flowing through the coil and the Lorentz force acting on the workpiece.

In section 1.4 we describe the numerical tools used to obtain the electromagnetic fields and the deformation of the workpiece.

In section 1.5 and 1.6 we apply the method detailed in section 1.3 to the bulging of a metal sheet and the bulging of a cylindrical tube. Our results are compared with theoretical predictions and measurements found in the literature.

In section 1.7 we explain how to estimate the optimum frequency and capacitance at which it is attained the maximum workpiece deformation for a given initial energy and a given set of coil and workpiece.

Finally, in section 1.8 we apply the techniques detailed in section 1.7 to a tube bulging process and to a tube compression process.

1.2 Coupling strategies

EMF is fundamentally an electro-thermo-mechanical process. Different coupling strategies have been proposed to solve numerically this multi-physics problem, but they can be reduced to these three categories: direct or monolithic coupling, sequential coupling and loose coupling.

The direct or monolithic coupling [24, 13] consists in solving the full set of field equations every time step. This approach is the most accurate but it does not take advantage of the different time scales characterizing electromagnetic, mechanical and thermal transients. Moreover, the linear system resulting from the numerical discretization leads to large non-symmetric matrices which are computationally expensive to solve and made this approach unpractical.

In the sequential coupling strategy [7, 17, 27, 20, 9] the EMF process is divided into three sub-problems (electromagnetic, thermal and mechanical) and each field is evolved keeping the others fixed. Usually the process is considered adiabatic and it only alternates the solution of the electromagnetic and the mechanical equations. That is, the Lorentz forces are first calculated and then automatically transferred as input load to the mechanical model. The mechanical model deforms the workpiece and, thereafter, the geometry of the electromagnetic model is updated and so on. These iterations are repeated until the end of the EMF process. The advantages of this method is that it is very accurate and it can be made computationally efficient.

In the loose coupling strategy [14] the Lorentz forces are calculated neglecting the workpiece deformation. Then, they are transferred to the mechanical model which uses them as a driven force to deform the workpiece. This approach is less accurate than the former methods but it is computationally the most efficient and it can be very useful for estimating the order of magnitude of the parameters of an EMF process, for experimentation on modeling conditions or for modeling complex geometries. Also, it provides results as accurate as the other strategies when applied to small deformations or abrupt magnetic pressure pulses. In [1, 26, 12] it is shown a comparative performance of this approach with the sequential coupling strategy.

In this work we perform all the electromagnetic computations neglecting the workpiece deformation. This is done for clarity reasons and also because the results obtained with a static, un-deformed workpiece are useful for a rough estimation of the parameters involved in an EMF process. Moreover, the usual uncertainties in the knowledge of some parameters (mechanical properties of the workpiece, electrical properties of the RLC circuit, etc) can overshadow any improvement generated by the computationally more expensive sequential coupling.

On the other hand, if we have a precise knowledge of all the EMF parameters and we want to improve the accuracy of the simulations then, we can consider our results as the first step of a sequential coupling strategy. That is, we transfer the force calculated on the un-deformed workpiece to the mechanical model. The mechanical model deforms the workpiece until it reaches some prefixed value. Then, we input the new geometry into the electromagnetic model and so on.

In this sequential strategy is not necessary to solve the electromagnetic equations each time step. It is only necessary to solve them when the deformation of the workpiece produces appreciable changes in the electromagnetic parameters of the system coil-workpiece (inductance, resistance and Lorentz force). Therefore, we do not have to worry about numerical instabilities caused by a wrong choice of the time step.

1.3 Electromagnetic model

The electromagnetic model followed in the present work starts by solving the time-harmonic Maxwell's equations in a frequency interval. For each frequency ω we compute the electromagnetic fields inside a volume v containing the coil and the workpiece. With $\mathbf{E}(\mathbf{r},\omega)$ and $\mathbf{H}(\mathbf{r},\omega)$ we compute the inductance $L_{cw}(\omega)$ and the resistance $R_{cw}(\omega)$ of the system coil-workpiece. With $L_{cw}(\omega)$ and $R_{cw}(\omega)$ we obtain the intensity $I(t)$ flowing through the coil. Finally, with $I(t)$ and the magnetic field $\mathbf{H}(\mathbf{r},\omega)$ on the surfaces of the workpiece we can calculate the Lorentz force that drives the EMF process.

In section 1.3.2 we explain how to compute the inductance $L_{cw}(\omega)$ and the resistance $R_{cw}(\omega)$ with the electromagnetic fields $\mathbf{E}(\mathbf{r},\omega)$ and $\mathbf{H}(\mathbf{r},\omega)$.

In section 1.3.4 we show how to obtain the intensity $I(t)$ with the calculated values of $L_{cw}(\omega)$ and $R_{cw}(\omega)$.

Finally, in sections 1.3.5 and 1.3.6 we compute the Lorentz force acting on the workpiece with the Fourier transform of $I(t)$ and $\mathbf{H}(\mathbf{r},\omega)$.

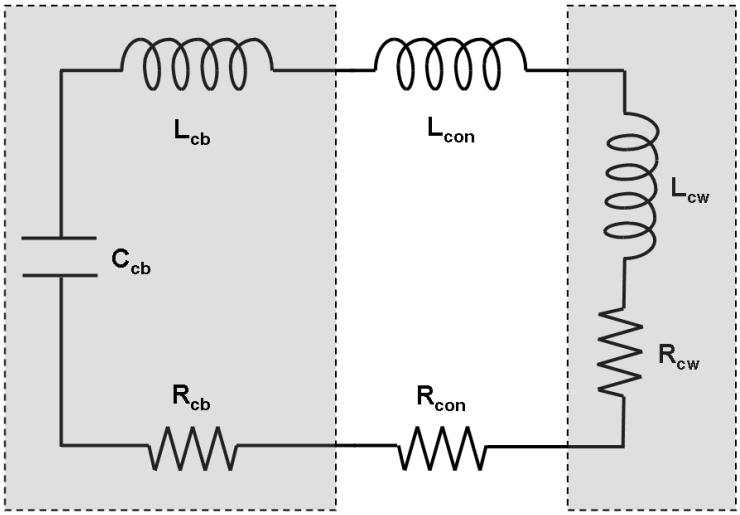

Figure 1.1: RLC circuit used to produce the discharge current. In the shadowed rectangle at the left is represented the capacitor bank with capacitance C_{cb}, inductance L_{cb} and resistance R_{cb}. In the shadowed rectangle at the right is represented the system formed by the coil and the metal workpiece. This system has an inductance L_{cw} and a resistance R_{cw}. Between both rectangles are represented the cables connecting the capacitor bank with the coil. These cables have an inductance L_{con} and a resistance R_{con}.

1.3.1 Input data

The input data required for computing the Lorentz force are:

a) Geometry and material properties of the coil and the workpiece.

b) Electrical parameters of the capacitor bank (capacitance C_{cb}, inductance L_{cb}, resistance R_{cb} and initial voltage V_0).

c) Electrical parameters of the cables connecting the coil with the capacitor bank (inductance L_{con} and resistance R_{con}).

From the data in a) we calculate the inductance L_{cw} and the resistance R_{cw} of the system coil-workpiece as a function of the frequency ω. With $L_{cw}(\omega)$ and $R_{cw}(\omega)$ and the data in b) and c)

we find the intensity $I(t)$ flowing through the RLC circuit of fig. 1.1. Finally, with $I(t)$ and the magnetic field calculated with the data in a) we obtain the Lorentz force acting on the workpiece. In the following we analyze these steps in more detail.

1.3.2 Inductance and resistance of the system coil-workpiece

The repulsive force between the coil and the workpiece is a consequence of the time varying current $I(t)$ generated in the RLC circuit of fig. 1.1. To calculate $I(t)$ we first need the values of the inductance L_{cw} and the resistance R_{cw}. We do not take into account the capacitance of the system coil-workpiece because it is negligible in the geometries and at the frequencies usually involved in electromagnetic forming. The same is applicable to the capacitance of the cables connecting the coil with the capacitor bank.

We consider the set coil-workpiece as a generic, two-terminal, linear, passive electromagnetic system operating at low frequencies. We can imagine the coil and the workpiece inside a volume υ with only its input terminals protruding. Under these assumptions, the inductance L_{cw} and the resistance R_{cw} at the frequency ω can be calculated with [11]

$$L_{cw}(\omega) = \frac{1}{|I_n|^2} \int_{\upsilon} \mu |\mathbf{H}(\mathbf{r}, \omega)|^2 \, d\upsilon, \tag{1.1}$$

$$R_{cw}(\omega) = \frac{1}{|I_n|^2} \int_{\upsilon} \sigma |\mathbf{E}(\mathbf{r}, \omega)|^2 \, d\upsilon \tag{1.2}$$

where I_n is the current injected into the system through the input terminals, μ is the magnetic permeability, $\mathbf{H}(\mathbf{r}, \omega)$ is the magnetic field, σ is the electrical conductivity and $\mathbf{E}(\mathbf{r}, \omega)$ is the electric field. The fields $\mathbf{E}(\mathbf{r}, \omega)$ and $\mathbf{H}(\mathbf{r}, \omega)$ are obtained after solving the time-harmonic Maxwell's equations at a given frequency ω. For each frequency ω we have a different value of L_{cw} and R_{cw}. The injected current I_n is a dummy variable that is only used to drive the problem. It can take any value without affecting the final result of (1.1) and (1.2).

1.3.3 Intensity in the RLC circuit

In fig. 1.1 is shown a typical RLC circuit used in electromagnetic forming. This circuit has a resistance R, an inductance L and a capacitance C given by

$$\begin{aligned} R &= R_{cb} + R_{con} + R_{cw}, \\ L &= L_{cb} + L_{con} + L_{cw}, \\ C &= C_{cb}. \end{aligned} \tag{1.3}$$

The values of R and L vary with time because of the deformation of the workpiece. In contrast, the capacitance C remain constant during all the forming process. The intensity $I(t)$ for all $t \in [0, \infty]$ flowing through the circuit of fig. 1.1 satisfies the differential equation

$$0 = \frac{d}{dt}(RI) + \frac{d}{dt}(L\frac{dI}{dt}) + \frac{1}{C}I, \tag{1.4}$$

with initial conditions $V(t_0) = V_0$ and $I(t_0) = 0$. The initial value V_0 represents the voltage at the terminals of the capacitor. This voltage is related with the energy of the discharge U_0 by

$$U_0 = \frac{1}{2} C V_0^2. \tag{1.5}$$

To find $I(t)$ with (1.4) we have to know first $R(t)$ and $L(t)$ for all $t \in [0, \infty]$.

If we consider a loose coupling strategy, the functions $R(t)$ and $L(t)$ are constants and equal to the values R_0 and L_0 calculated at the initial position with an un-deformed workpiece. Therefore, we have that $R(t) = R_0$ and $L(t) = L_0$ for all $t \in [0, \infty]$. Under these circumstances, the solution of (1.4) is given by

$$I(t) = \frac{V_0}{\omega_0 L_0} e^{-\gamma_0 t} \sin(\omega_0 t), \tag{1.6}$$

where

$$\omega_0 = 2\pi\nu_0 = \sqrt{\frac{1}{L_0 C} - \left(\frac{R_0}{2L_0}\right)^2} \tag{1.7}$$

and

$$\gamma_0 = \frac{R_0}{2L_0}. \tag{1.8}$$

If we consider a sequential coupling strategy then we solve (1.4) in time intervals $[t_i, t_{i+1}]$. This time intervals correspond with the time periods between two successive calls to the electromagnetic equations. We can assume that $L(t)$ and $R(t)$ are constants inside each $[t_i, t_{i+1}]$ and equal to the values R_i and L_i calculated with the deformed workpiece at t_i. In a sequential coupling strategy , the expression (1.6) is the solution of the first time interval $[t_0, t_1]$.

1.3.4 Capacitance and frequency

Equation (1.6) shows that if we want to know the intensity $I(t)$ we have to know first the values of ω_0, C, V_0, L_0 and R_0. The capacitance C and the voltage V_0 are given data. The inductance L_0 and the resistance R_0 can be obtained with the help of (1.1), (1.2) and (1.3). The only value that remains unknown is ω_0.

The frequency ω_0 is determined by the capacitance C_{cb} for a given set of coil, workpiece and connectors. The frequency ω_0 is the solution of the implicit equation

$$C_0(\omega) - C_{cb} = 0, \tag{1.9}$$

where the relation $C_0(\omega)$ is obtained after reordering expression (1.7)

$$C_0(\omega) = \frac{4L_0(\omega)}{4\omega^2 L_0(\omega)^2 + R_0(\omega)^2}. \tag{1.10}$$

In the case of using a sequential coupling strategy, we must take into account that the functions $L_i(\omega)$ and $R_i(\omega)$ are different in each $[t_i, t_{i+1}]$ and, as a consequence, the frequency ω_i is also different in each time interval.

1.3.5 Lorentz force on the workpiece

To calculate the electromagnetic force acting on the workpiece we made the following assumptions:

i) The dimensions of the system coil-workpiece are small compared with the wavelength of the prescribed fields. The wavelengths involved in EMF are in the order of $\lambda \approx 10^3 - 10^5$ m with frequencies in the order of $\nu \approx 10^3 - 10^4$ Hz. As a consequence of this, we can consider the displacement current negligible $\partial \mathbf{D}/\partial t \approx 0$ and to treat the fields as if they propagated instantaneously with no appreciable radiation [23, 11].

ii) The workpiece is linear, isotropic, homogeneous and non-magnetic ($\mu = \mu_0$). These properties represent all the workpieces used in this work (aluminium alloys). If we want to consider more complex materials, we must add to (1.11) the surface and volumetric integrals described in [23].

iii) The modulus of the velocity at any point in the workpiece is always much less than $|\mathbf{v}| << 10^7$ m/s. In fact, the velocities involved in EMF are in the order of $|\mathbf{v}| \approx 10^2 - 10^3$ m/s. This circumstance allows us to neglect the velocity terms that appear in the Maxwell's equations when working with moving media [15].

Under hypothesis i)-iii) we can express the total force acting on the workpiece by [16]

$$\mathbf{F} = \int_{\upsilon} \mathbf{f}_{\upsilon} \, d\upsilon = \int_{\upsilon} (\mathbf{J} \times \mathbf{B}) \, d\upsilon, \tag{1.11}$$

where $\mathbf{f}_{\upsilon}$ is a volumetric force density, $\mathbf{J} = \sigma \mathbf{E}$ is the current density induced in the workpiece and $\mathbf{B} = \mu_0 \mathbf{H}$ is the magnetic flux density. If we use the vector identity

$$\mathbf{B} \times \nabla \times \mathbf{B} = \nabla \left(\frac{1}{2} |\mathbf{B}|^2 \right) - (\mathbf{B} \cdot \nabla) \mathbf{B}, \tag{1.12}$$

and recalling that, by hypothesis i) and ii), the Ampere's circuital law is

$$\nabla \times \mathbf{B} = \mu_0 \mathbf{J}, \tag{1.13}$$

we can write the force density $\mathbf{f}_{\upsilon}$ as

$$\mathbf{f}_{\upsilon} = -\nabla \left(\frac{1}{2\mu_0} |\mathbf{B}|^2 \right) + \frac{1}{\mu_0} (\mathbf{B} \cdot \nabla) \mathbf{B}. \tag{1.14}$$

In EMF the last term of the right hand side is usually negligible compared with the first. This is so because the field $\mathbf{B}$ is almost unidirectional in the area of the workpiece just in front of the coil. In this area is where the main contribution to the total force is produced and also where the higher values of the Lorentz force are found. If a field $\mathbf{B}$ is unidirectional then, by the Gauss law for magnetism ($\nabla \cdot \mathbf{B} = 0$), it will not change in the direction of $\mathbf{B}$. If a field $\mathbf{B}$ only changes in the directions perpendiculars to $\mathbf{B}$ then we have that $(\mathbf{B} \cdot \nabla) \mathbf{B} = 0$. In other words, to neglect the

last term of (1.14) is equivalent to neglect the compressive and expansive forces parallels to the workpiece surface and to state that, in EMF, the Lorentz force is due to the change in magnitude of the magnetic field along the thickness of the workpiece. Therefore, in EMF, we can simplify (1.14) to

$$\mathbf{f}_\upsilon \approx -\nabla \left(\frac{1}{2\mu_0} |\mathbf{B}|^2 \right). \tag{1.15}$$

Sometimes, the computational codes that solve the mechanical equations work more easily with pressures than with volumetric forces densities. In such cases, it is advantageous to express the force acting on the workpiece as a magnetic pressure applied on its surface. This magnetic pressure is the line integral of (1.15) from a point $\mathbf{r}_0$ placed on the workpiece surface nearest to the coil to a point $\mathbf{r}_\tau$ placed on the opposite side of the workpiece. The path to follow is a straight line with a direction defined by the surface normal at $\mathbf{r}_0$. The magnetic pressure is then given by

$$P(\mathbf{r}_0, t) = \int_{\mathbf{r}_0}^{\mathbf{r}_\tau} \mathbf{f}_\upsilon \, d\mathbf{s} = \frac{1}{2\mu_0} \left(|\mathbf{B}(\mathbf{r}_0, t)|^2 - |\mathbf{B}(\mathbf{r}_\tau, t)|^2 \right), \tag{1.16}$$

which it can be also expressed as a function of $\mathbf{H}$ recalling that, by hypothesis (ii), $\mathbf{B} = \mu_0 \mathbf{H}$

$$P(\mathbf{r}_0, t) = \frac{1}{2} \mu_0 \left(|\mathbf{H}(\mathbf{r}_0, t)|^2 - |\mathbf{H}(\mathbf{r}_\tau, t)|^2 \right). \tag{1.17}$$

We can conclude from equation (1.17) that, under hypothesis i)-iii), we only need to know $|\mathbf{H}(\mathbf{r}, t)|$ on the surfaces of the workpiece to characterize electromagnetically the EMF process.

1.3.6 Lorentz force in frequency domain

The fields $\mathbf{H}(\mathbf{r}, t)$ of (1.17) can be represented in frequency domain using the inverse Fourier transform as follows

$$\mathbf{H}(\mathbf{r}, t) = \frac{1}{2\pi} \int_{-\infty}^{\infty} \left[\mathbf{H}_n(\mathbf{r}, \omega) \, I(\omega) \right] \, e^{i\omega t} \, d\omega, \tag{1.18}$$

where $i = \sqrt{-1}$ is the imaginary unit, $\mathbf{H}_n(\mathbf{r}, \omega)$ is the magnetic field per unit intensity at the frequency ω and $I(\omega)$ is the Fourier transform of the intensity $I(t)$ flowing through the RLC circuit

$$I(\omega) = \int_{-\infty}^{\infty} I(t) \, e^{-i\omega t} dt. \tag{1.19}$$

If the intensity $I(t)$ is given by (1.6) then the analytical expression of $I(\omega)$ is

$$I(\omega) = \frac{1}{2} \left(\frac{1}{\omega + \omega_0 - i\gamma_0} - \frac{1}{\omega - \omega_0 - i\gamma_0} \right), \tag{1.20}$$

where ω_0 is the frequency (1.7) and γ_0 is defined in (1.8). The magnetic field per unit intensity $\mathbf{H}_n(\mathbf{r}, \omega)$ is defined by

$$\mathbf{H}_n(\mathbf{r}, \omega) = \frac{\mathbf{H}(\mathbf{r}, \omega)}{I_n}, \tag{1.21}$$

where $\mathbf{H}(\mathbf{r}, \omega)$ and I_n are the same magnetic field and intensity as the ones appearing in (1.1).

We can write the Fourier transform of $\mathbf{H}(\mathbf{r}, t)$ as it is shown in (1.18) because, by hypothesis i) and ii), we are in the quasi-static regime and in the presence of linear materials. This implies that the magnetic field has almost a constant phase inside the system coil-workpiece and that it is linearly related with the current intensity. Also, it implies that the magnetic field and the current are in phase and, as a consequence, $\mathbf{H}_n(\mathbf{r}, \omega)$ is approximately a real number $\mathbf{H}_n(\mathbf{r}, \omega) \approx Real\,[\mathbf{H}_n(\mathbf{r}, \omega)]$. The advantage of using $\mathbf{H}_n(\mathbf{r}, \omega)$ is that we can know the magnetic field inside the system coil-workpiece for any value of the current intensity $I(\omega)$ once it is known for I_n.

1.4 Numerical analysis tools

Two different numerical tools are used to simulate the electromagnetic forming process. One solves the electromagnetic equations and the other solves the mechanical equations. The input data a)-c) (section 1.3.1) are provided to the electromagnetic code to obtain the magnetic pressure (1.17) on the surfaces of the workpiece. Afterwards, this magnetic pressure is provided to the mechanical code to obtain the deformation workpiece.

The electromagnetic equations are solved with the in-house code ERMES. The numerical formulation behind ERMES is explained in detail in [18].

The mechanical equations are solved with the commercial software STAMPACK [22]. This numerical tool has been applied to processes such as ironing, necking, embossing, stretch-forming, forming of thick sheets, flex-forming, hydro-forming, stretch-bending of profiles, etc. It can solve dynamic problems with high speeds and large strains rates, obtaining explicitly accelerations, velocities and deformations. In this work, our emphasis is on the electromagnetic part of the EMF process, then, we do not go further into the numerical formulation behind STAMPACK. For a detailed information about this formulation see [3].

1.5 Application example I. Sheet bulging.

In this section we apply the electromagnetic model explained above to the EMF process presented in [25]. This process consists in the free bulging of a thin metal sheet by a spiral flat coil. Our objective is to find the magnetic pressure acting on the workpiece for the given value of the capacitance $C_{cb} = 40\,\mu$F and the initial voltage $V_0 = 6\,$kV.

1.5.1 Description of the system coil-workpiece

The spiral flat coil appearing in [25] can be approximated by coaxial loop currents in a plane. Thus, the problem can be considered axis symmetric. The dimensions of the coil and the workpiece are shown in fig. 1.2. The diameter of the wire, material properties and horizontal positioning of the coil are missed in [25]. We used the values given in [7], where the same problem is treated and it is provided a complete description of the geometry.

The coil is made of copper with an electrical conductivity of $\sigma = 58e6$ S/m. The workpiece is a circular plate of annealed aluminum JIS A 1050 with an electrical conductivity of $\sigma = 36e6$ S/m.

It is assumed $\epsilon = \epsilon_0$ and $\mu = \mu_0$ in the coil and in the workpiece.

The RLC circuit has an inductance $L_{cb} + L_{con} = 2.0\,\mu$H, a resistance $R_{cb} + R_{con} = 25.5\,\mathrm{m}\Omega$ and a capacitance $C_{cb} = 40\,\mu$F. The capacitor bank was initially charged with a voltage of $V_0 = 6\,$kV.

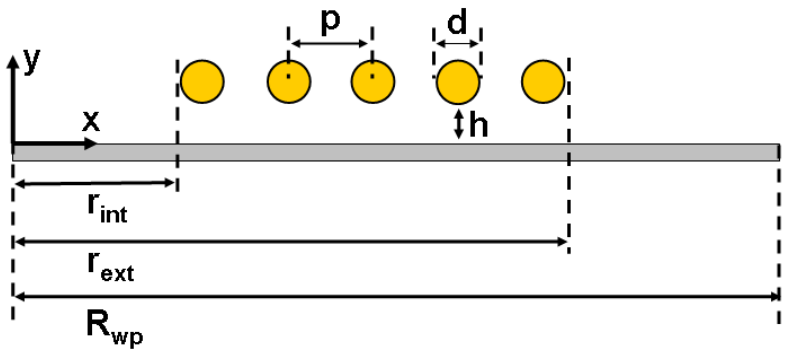

Figure 1.2: Dimensions of the system coil-workpiece. Data taken from [25, 7]. Number of turns of the coil $N = 5$. Pitch or coil separation $p = 5.5$ mm. Diameter of the coil wires $d = 1.29$ mm (16 AWG). Maximum coil radius $r_{ext} = 32$ mm. Minimum coil radius $r_{int} = 8.71$ mm. Separation distance between coil and metal sheet $h = 1.6$ mm. Thickness of the sheet $\tau = 0.5$ mm. Radius of the workpiece $R_{wp} = 55$ mm.

1.5.2 Finite element model

Although, undoubtedly, in this case the best option is to perform the computations with an axis symmetric two-dimensional computational tool, we used the in-house three-dimensional code ERMES. The advantages are that we do not need to build a new tool and that we can solve more general situations with the same software and the same file exchange interface between ERMES and STAMPACK. On the other hand, for this specific problem, our tools are computationally less efficient.

We employed the geometry shown in fig. 1.3 to compute the electromagnetic fields with ERMES. The geometry is a truncated portion of a sphere with an angle of 20°. We drive the problem with a current density **J** uniformly distributed in the volume of the coil wires. In the colored surfaces of fig. 1.3 we imposed the regularized perfect electric conductor (PEC) boundary conditions (see chapter 3)

$$\begin{aligned} \nabla \cdot (\varepsilon \mathbf{E}) &= 0, \\ \hat{\mathbf{n}} \times \mathbf{E} &= 0. \end{aligned} \tag{1.22}$$

It is not necessary to impose more boundary condition if we apply in all the FEM nodes of the domain a change of coordinates from cartesian (E_x, E_y, E_z) to axis symmetric around the Y axis (E_ρ, E_φ, E_y). That is, at the same time we are building the matrix, we enforce at each node of the

FEM mesh the following

$$\begin{pmatrix} E_\rho \\ E_\varphi \\ E_y \end{pmatrix} = \begin{pmatrix} x/\rho & 0 & z/\rho \\ -z/\rho & 0 & x/\rho \\ 0 & 1 & 0 \end{pmatrix} \begin{pmatrix} E_x \\ E_y \\ E_z \end{pmatrix} \tag{1.23}$$

where x and z are the cartesian coordinates of the node and $\rho = \sqrt{x^2 + z^2}$. We preserve the symmetry of the final FEM matrix applying (1.23) and its transpose as it is explained in [2].

The advantage of using (1.23) is that $E_\rho = 0$ and $E_y = 0$ in axis symmetric problems. This fact reduces by a factor of three the size of the final matrix and also the time required to solve it. Therefore, we can improved noticeably the computational performance of ERMES in axis symmetric problems with a simple modification of its matrix building procedure. In a desktop computer with a CPU Intel Core 2 Quad Q9300 at 2.5 GHz and the operative system Microsoft Windows XP, ERMES requires less than 30 s and less than 500 MB of memory RAM to solve each frequency.

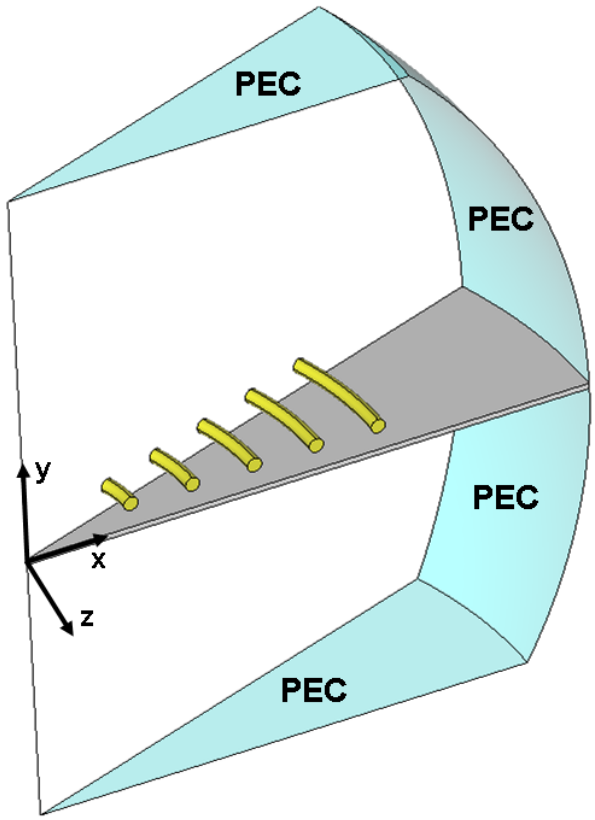

Figure 1.3: Geometry used in ERMES to compute the electromagnetic fields in the free bulging process of a thin metal sheet by a spiral flat coil.

1.5.3 Intensity through the RLC circuit

Once the initial geometry of system coil-workpiece is properly characterized, we have to find the intensity $I(t)$ flowing through the RLC circuit. As it is mentioned in section 1.3.4, if we want to know $I(t)$ we have to calculate first the frequency ω_0. This frequency ω_0 is the solution of equation (1.9) with $C_{cb} = 40\,\mu$F. We solved (1.9) using the following iterative procedure:

1) We replace in $C_0(\omega)$ the frequency which satisfies $\delta = \tau$, where τ is the thickness of the workpiece and δ is the skin depth
$$\delta = \sqrt{\frac{1}{\pi\nu\mu\sigma}}. \tag{1.24}$$

2) We compare $C_0(\omega)$ with C_{cb}. If $C_0(\omega) > C_{cb}$ then we must increase the value of ω. If $C_0(\omega) < C_{cb}$ then we must decrease the value of ω. If $C_0(\omega) = C_{cb}$ then we have found the solution ω_0.

3) If the solution is not achieved then we replace in $C_0(\omega)$ the new incremented/decremented value of ω and go to step 2). The procedure is repeated until the solution is achieved.

In fig. 1.4 is shown the capacitance C_0 as a function of the frequency ν and the solution $\nu_0 = 16.35\,$kHz for the given capacitance $C_{cb} = 40\,\mu$F. We have choose an initial frequency satisfying $\delta = \tau$ because we have observed in the literature that the typical frequencies employed in EMF lay in the interval
$$0.5 < \frac{\delta}{\tau} < 1.5. \tag{1.25}$$
In the present case, we have that the skin depth is $\delta = 1.3\,\tau$.

As it is indicated in equation (1.10), we need to know $L_0(\omega)$ and $R_0(\omega)$ to calculate $C_0(\omega)$. These functions are defined in (1.3) and they represent the total inductance and the total resistance of the RLC circuit of fig. 1.1. We assume that the given values $L_{cb} + L_{con} = 2.0\,\mu$H and $R_{cb} + R_{con} = 25.5\,m\Omega$ do not change with the frequency. On the other hand, L_{wp} and R_{wp} are frequency dependant and they have to be calculated with the help of (1.1) and (1.2). In the volume of the coil, equation (1.2) is replaced by
$$R_{cw}(\omega) = \frac{1}{|I_n|^2}\int_{\upsilon} \frac{|\mathbf{J}|^2}{\sigma}\, d\upsilon \tag{1.26}$$
where $\mathbf{J}$ is the imposed current density and σ is the conductivity of the coil. We recall that if we want to obtain a volume integral for all the space then we must multiply by 18 (=360°/20°) any volume integral calculated in the portion of truncated sphere of fig. 1.3. The values of the total inductance L_0 and the total resistance R_0 as a function of the frequency ν are shown in fig. 1.5 and in fig. 1.6.

If we substitute in equation (1.6) the calculated values of $\omega_0 = 2\pi\nu_0$, $L_0(\omega_0) = 2.35\,\mu$H and $R_0(\omega_0) = 38.1\,$mΩ and the given values of C_{cb} and V_0 then we obtain the intensity $I(t)$ flowing through the coil. In fig. 1.7 we compare the intensity calculated in [25] with the intensity calculated in this work.

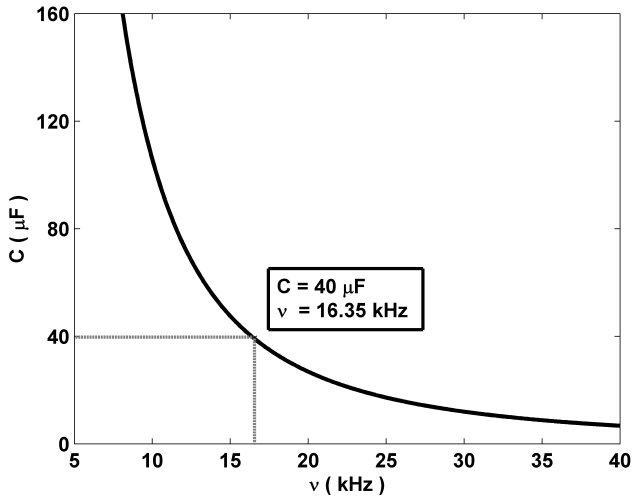

Figure 1.4: Capacitance C_0 as a function of the frequency ν for the un-deformed workpiece placed in its initial position. The function $C_0(\nu)$ is obtained from equation (1.10). If the capacitor bank has a $C_{cb} = 40\,\mu$F the oscillation frequency of the RLC circuit is $\nu_0 = 16.35\,$kHz.

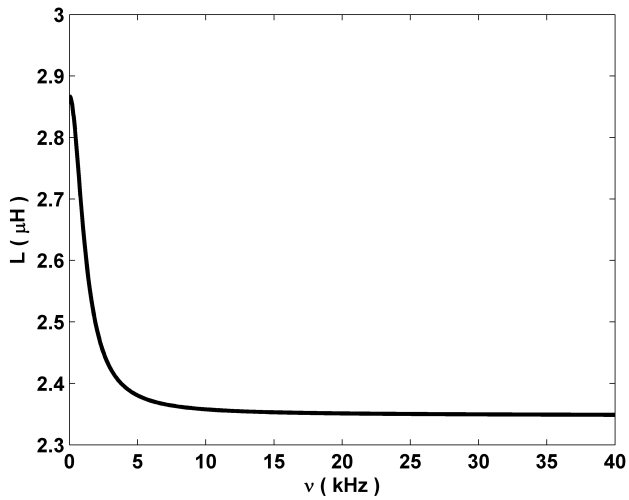

Figure 1.5: Total inductance $L_0 = L_{cb} + L_{con} + L_{cw}$ as a function of the frequency ν for the un-deformed workpiece placed in its initial position. The inductance of the system coil-workpiece L_{cw} is calculated with the equation (1.1). The value of L_{cw} varies from $0.86\,\mu$H at the lower frequencies to $0.35\,\mu$H at the higher frequencies. We assumed that the inductance of the exterior circuit $L_{cb} + L_{con} = 2.0\,\mu$H remains constant in this frequency band.

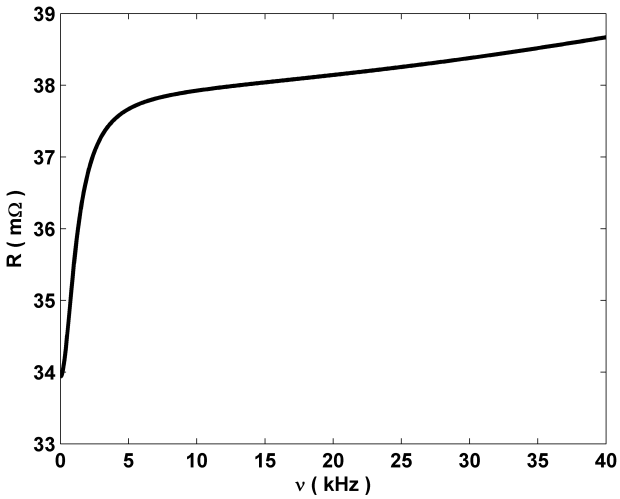

Figure 1.6: Total resistance $R_0 = R_{cb} + R_{con} + R_{cw}$ as a function of the frequency ν for the un-deformed workpiece placed in its initial position. The resistance of the system coil-workpiece R_{cw} is calculated with equation (1.2) in the volume of the workpiece and with equation (1.26) in the volume of the coil. The value of R_{cw} varies from $8.4\,\mathrm{m}\Omega$ at the lower frequencies to $13.2\,\mathrm{m}\Omega$ at the higher frequencies. We assumed that the resistance of the exterior circuit $R_{cb} + R_{con} = 25.5\,\mathrm{m}\Omega$ remains constant in this frequency band.

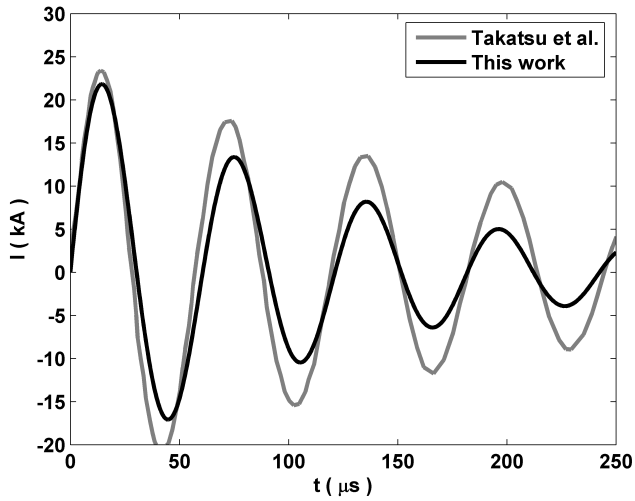

Figure 1.7: Intensity calculated in Takatsu et al. [25] compared with the intensity calculated in this work. We have graphed expression (1.6) with $V_0 = 6\,\mathrm{kV}$, $C_{cb} = 40\,\mu\mathrm{F}$, $\nu_0 = 16.35\,\mathrm{kHz}$, $\omega_0 = 2\pi\nu_0$, $L_0 = 2.35\,\mu\mathrm{H}$ and $R_0 = 38.1\,\mathrm{m}\Omega$.

1.5.4 Magnetic pressure on the workpiece

If we want to calculate the magnetic pressure (1.17) acting on the workpiece then we need the fields $\mathbf{H}(\mathbf{r}_0, t)$ and $\mathbf{H}(\mathbf{r}_\tau, t)$, where $\mathbf{r}_0$ is located on the surface of the workpiece nearest to the coil (S_0) and $\mathbf{r}_\tau$ is located on the surface of the workpiece farthest to the coil (S_τ). The fields $\mathbf{H}(\mathbf{r}_0, t)$ and $\mathbf{H}(\mathbf{r}_\tau, t)$ are obtained from (1.18) with the Fourier transform of $I(t)$ and the magnetic fields per unit intensity $\mathbf{H}_n(\mathbf{r}_0, \omega)$ and $\mathbf{H}_n(\mathbf{r}_\tau, \omega)$. In fig. 1.8 are shown $|\mathbf{H}_n(\mathbf{r}_0, \omega)|$ and $|\mathbf{H}_n(\mathbf{r}_\tau, \omega))|$ as a function of the frequency ν. In fig. 1.9 are shown $|\mathbf{H}_n(\mathbf{r}_0, \omega_0)\, I(\omega)|$, $|\mathbf{H}_n(\mathbf{r}_0, \omega))\, I(\omega)|$ and $|\mathbf{H}_n(\mathbf{r}_\tau, \omega))\, I(\omega)|$ as a function of the frequency ν. It can be shown (see fig. 1.9) that, in this EMF process, we have

$$\begin{aligned} \mathbf{H}_n(\mathbf{r}_0, \omega_0)\, I(\omega) &\approx \mathbf{H}_n(\mathbf{r}_0, \omega)\, I(\omega), \\ |\mathbf{H}_n(\mathbf{r}_0, \omega_0)\, I(\omega)| &\gg |\mathbf{H}_n(\mathbf{r}_\tau, \omega)\, I(\omega)|. \end{aligned} \tag{1.27}$$

If we use (1.27) in (1.18) and (1.17) then we can write the magnetic pressure $P(\mathbf{r}_0, t)$ as

$$P(\mathbf{r}_0, t) = \frac{1}{2}\, \mu_0 |\mathbf{H}_n(\mathbf{r}_0, \omega_0)\, I(t)|^2. \tag{1.28}$$

This simplification of (1.17), which is possible when (1.27) is accomplished, is very useful in a sequential coupling strategy. This is so because, in the next calls to the electromagnetic model, we will only need to find the magnetic field for one frequency, which makes the computations more efficient.

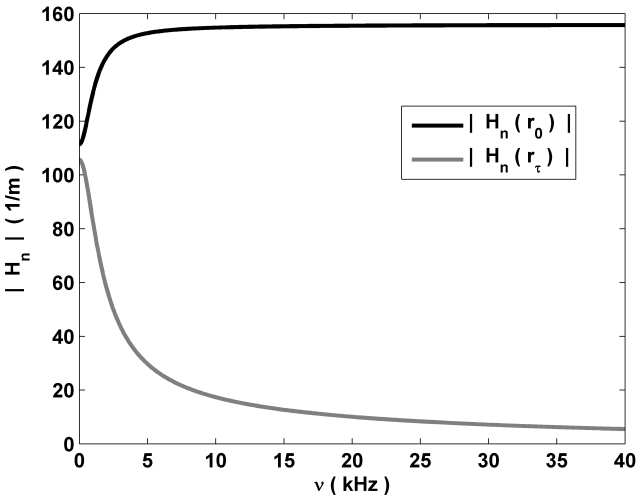

Figure 1.8: Modulus of the magnetic fields per unit intensity $|\mathbf{H}_n(\mathbf{r}_0, \omega)|$ and $|\mathbf{H}_n(\mathbf{r}_\tau, \omega)|$ as a function of the frequency ν. The point $\mathbf{r}_0$ is located on S_0. The point $\mathbf{r}_\tau$ is located on S_τ, on the opposite side of where $\mathbf{r}_0$ is placed.

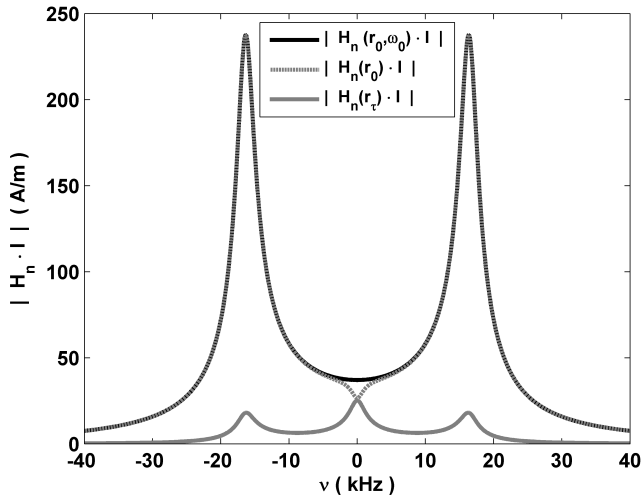

Figure 1.9: Modulus of the magnetic fields $|\mathbf{H}_n(\mathbf{r}_0, \omega_0)\, I(\omega)|$, $|\mathbf{H}_n(\mathbf{r}_0, \omega)\, I(\omega)|$ and $|\mathbf{H}_n(\mathbf{r}_\tau, \omega)\, I(\omega)|$ as a function of the frequency ν. The constant $\mathbf{H}_n(\mathbf{r}_0, \omega_0)$ is the magnetic field per unit intensity at the frequency ω_0 in the point $\mathbf{r}_0$. The point $\mathbf{r}_0$ is located on S_0. The function $I(\omega)$ is the Fourier transform of the intensity $I(t)$. The analytical expression of $I(\omega)$ is given by (1.20). The function $\mathbf{H}_n(\mathbf{r}_0, \omega)$ is the magnetic field per unit intensity at the point $\mathbf{r}_0$. The function $\mathbf{H}_n(\mathbf{r}_\tau, \omega)$ is the magnetic field per unit intensity at the point $\mathbf{r}_\tau$. The point $\mathbf{r}_\tau$ is located on S_τ, on the opposite side of where $\mathbf{r}_0$ is placed. In this graph we can see that $|\mathbf{H}_n(\mathbf{r}_0, \omega_0)\, I(\omega)| \approx |\mathbf{H}_n(\mathbf{r}_0, \omega)\, I(\omega)|$ and $|\mathbf{H}_n(\mathbf{r}_0, \omega_0)\, I(\omega)| \gg |\mathbf{H}_n(\mathbf{r}_\tau, \omega)\, I(\omega)|$.

In fig. 1.10 is shown the total magnetic force acting on the workpiece as a function of time. The total magnetic force is the integral of the function (1.28) over the whole surface S_0. We computed the total force using (1.28) with $\mathbf{H}_n(\mathbf{r}_0, \omega_0)$ and $I(t)$ calculated for the un-deformed workpiece placed in its initial position.

In fig. 1.11 is shown the radial distribution of the magnetic pressure (1.28) when the coil current reaches its maximum $I_{max} = 21.83\,\text{kA}$ at $t = 14.5\,\mu$s. In fig. 1.11 is also shown the magnetic pressure obtained in [25] when the coil current calculated there reaches its maximum at $t = 15.4\,\mu$s. In fig. 1.11 we see that, apart from a difference in the positioning of the coil, there is a difference in the magnitude of the magnetic pressure. The same difference is also observed in [21, 20], where this EMF process is simulated using two different approaches. One is based on FDTD (Finite Difference Time Domain) and the other on FEM (Finite Element Method). In the FDTD approach they used a similar procedure to that employed in [25]. In the FEM approach they used the freeware software FEMM4.0 [6]. In fig. 1.12 and fig. 1.13 we show the components of the magnetic flux density B_ρ and B_y calculated with FEMM4.0, FDTD and ERMES when the coil current is $I = 20.81\,\text{kA}$. In these figures we see that the results given by both FEM codes are similar between them but different from the results given by the FDTD method.

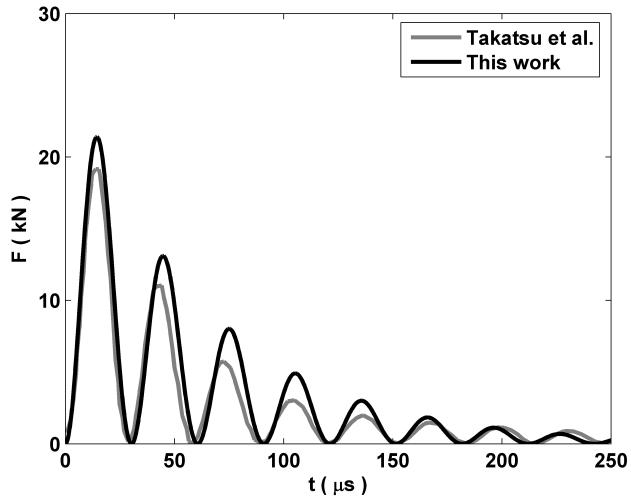

Figure 1.10: Total magnetic force calculated in Takatsu et al. [25] compared with the total magnetic force calculated in this work.

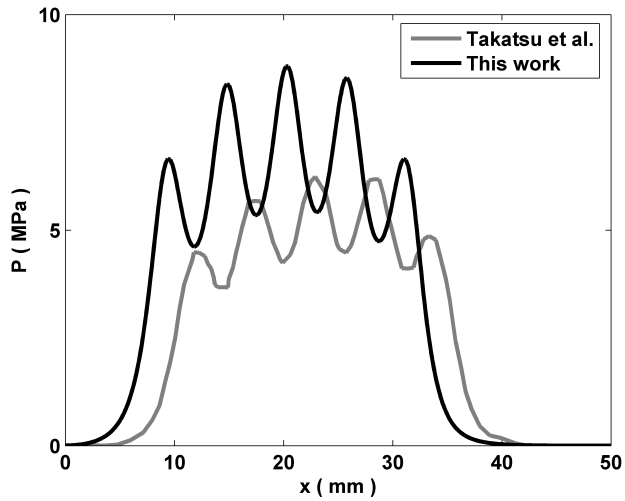

Figure 1.11: Radial distribution of the magnetic pressure calculated in Takatsu et al. [25] when the coil current reaches its maximum ($t = 15.4\,\mu$s) compared with the radial distribution of the magnetic pressure calculated in this work ($I_{max} = 21.83\,$kA at $t = 14.5\,\mu$s).

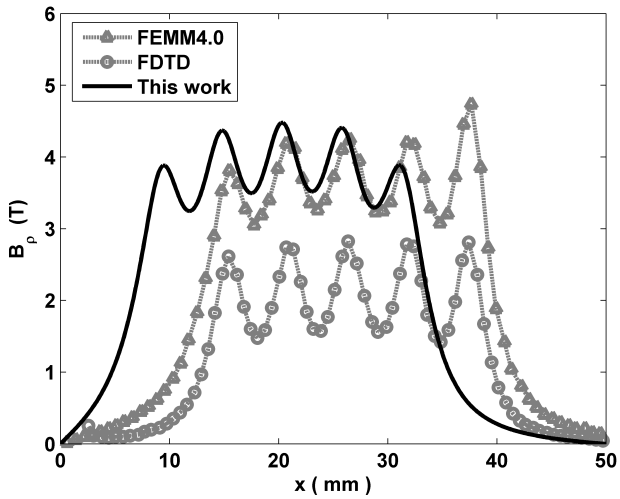

Figure 1.12: Radial component of the magnetic flux density calculated in [21] with FEM (FEMM4.0) and FDTD compared with the radial component of the magnetic flux density calculated in this work with ERMES.

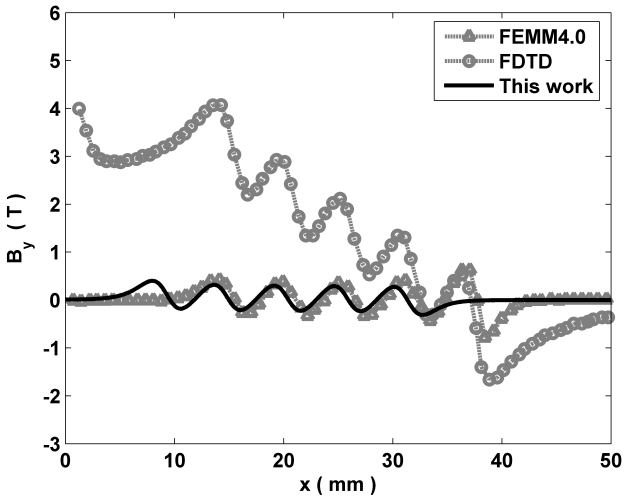

Figure 1.13: Axial component of the magnetic flux density calculated in [21] with FEM (FEMM4.0) and FDTD compared with the axial component of the magnetic flux density calculated in this work with ERMES.

The differences between the FDTD and the FEM approaches can be attributed to the use of a coarse mesh in the FDTD method. To show this, we solved a problem similar to the one appearing in this section (see fig. 1.2) but with a fixed workpiece of thickness $\tau = 3.0\,\text{mm}$, gap distance $h = 2.9\,\text{mm}$ and initial voltage $V_0 = 2\,\text{kV}$. We calculated in this set-up the radial component of the magnetic flux density B_ρ. Then, we compared our results with the simulations performed in [20] for different FDTD mesh sizes and also with the measurements of [25] (see fig. 1.14).

In fig. 1.14 we see that when the FDTD mesh is coarse (6 elements along the thickness of the sheet) the results of the FDTD simulations are in good agreement with the measurements but they are different from the results obtained with ERMES. On the hand, if we improve the FDTD mesh to 20 elements along the thickness of the sheet, the results of the FDTD simulations are similar to the results obtained with ERMES but they are different from the measurements. This unusual behavior can be explained if we consider that R_{con} and L_{con} are undervalued. If we add, for instance, only 1 meter of 16 AWG copper wire ($R_{1m} = 13.2\,\text{m}\Omega$, $L_{1m} = 1.5\,\mu\text{H}$ [8]) to the total resistance and the total inductance of the RLC circuit then, the results obtained with ERMES, and with the improved FDTD mesh, are in agreement with the measurements and also with the fact that improving the mesh must improve the results.

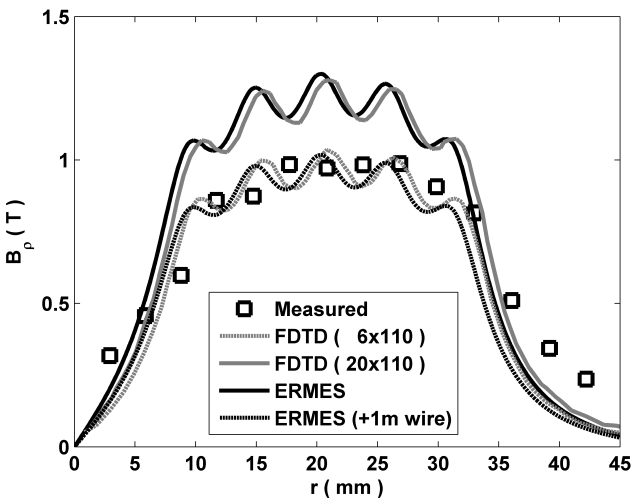

Figure 1.14: Radial component of the magnetic flux density B_ρ for the coil of fig. 1.2 with a fixed workpiece of thickness $\tau = 3.0\,\text{mm}$, gap distance $h = 2.9\,\text{mm}$ and initial voltage $V_0 = 2\,\text{kV}$. Measurements are from [25]. FDTD (6x110) represents the simulations performed in [20] with a FDTD mesh of 6 elements along the thickness of the sheet and 110 elements along the radial direction. FDTD (20x110) represents the simulations performed in [20] with a FDTD mesh of 20 elements along the thickness of the sheet and 110 elements along the radial direction. ERMES represents the simulations performed in this work. ERMES (+1m wire) represents the simulations performed in this work adding the DC resistance and the inductance of 1 meter of 16 AWG copper wire ($R_{1m} = 13.2\,\text{m}\Omega$, $L_{1m} = 1.5\,\mu\text{H}$ [8]) to the total inductance and the total resistance of the RLC circuit.

1.5.5 Deflection of the workpiece

We introduced in STAMPACK the magnetic pressure calculated in section 1.5.4 to obtain the deflection of the metal sheet. STAMPACK interprets the magnetic pressure as a mechanical pressure which deforms the workpiece. The results are shown in fig. 1.15.

In STAMPACK is not available the mechanical model used in [25]. Therefore, we had to adapt the parameters of the available model to reproduce the behavior of the material used in [25]. We considered the workpiece as an aluminium alloy with a Young's modulus $E = 69\,\text{GPa}$, density $\rho = 2700\,\text{Kg/m}^3$ and Poisson's ratio $\nu = 0.33$. STAMPACK used the Voce hardening law

$$\sigma_{cs} = \sigma_{y0} + (\sigma_m - \sigma_{y0})\left(1 - e^{-n\varepsilon_{ps}}\right), \tag{1.29}$$

where σ_{cs} is the Cauchy stress, $\sigma_{y0} = 34.9\,\text{MPa}$ is the yielding tensile strength, $\sigma_m = 128.8\,\text{MPa}$ is the ultimate tensile strength, $n = 12.0$ is the isotropic hardening parameter and ε_{ps} is the effective plastic deformation. STAMPACK also used a damping proportional to the nodal velocity ($\mathbf{F}_i = -\eta_i\,\mathbf{v}_i$) with $\eta_i = 2\alpha M_i$, being $\alpha = 138.6$ and M_i the lumped mass at the i-th node. The constant parameters of the mechanical model were obtained introducing in STAMPACK the magnetic pressure calculated in [25]. Then, we adjusted the parameters until achieve with STAMPACK the same deflection of the disk as the one measured in [25].

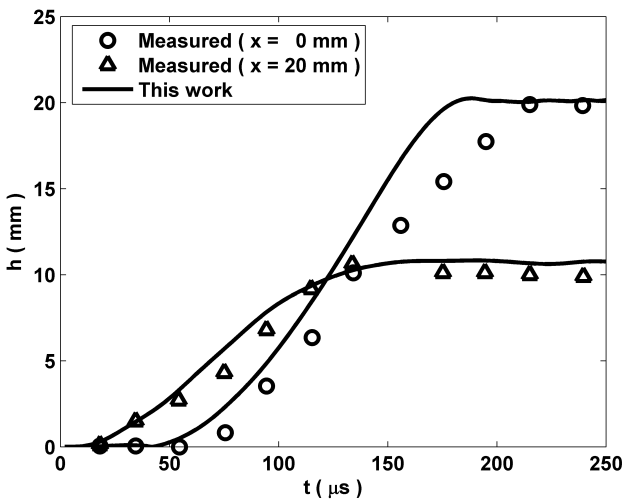

Figure 1.15: Deflection of the workpiece at the positions $x = 0\,\text{mm}$ and $x = 20\,\text{mm}$ as a function of time. The results of this work are compared with the measurements of Takatsu et al. [25].

1.6 Application example II. Tube bulging.

In this section we apply the electromagnetic model of section 1.3 to the EMF process presented in [28]. This process consists in the expansion of a cylindrical tube by a solenoidal coil. In [28] is analyzed the tube bulging process under different working conditions but, here, our objective is to find the magnetic pressure acting on the workpiece when the capacitance is $C_{cb} = 160\,\mu$F, the coil length is $\ell = 200$ mm and the initial charging energy is $U_0 = 2$ kJ.

1.6.1 Description of the system coil-workpiece

We take the geometrical description of the solenoidal coil and the tubular workpiece from [28]. The coil is approximated by coaxial loop currents, concentric with the workpiece and placed inside it. Thus, the problem is considered axis symmetric.

The coil is made of $d = 2.0$ mm diameter copper wire. The outer diameter of the coil is $D_c = 37.0$ mm. The separation between each loop is $p = 3.0$ mm. The length of the coil is approximately $\ell = 200$ mm and the number of turns is $N = 68$. We assume an electrical conductivity for copper of $\sigma = 58e6$ S/m.

The workpiece is a cylindrical tube made of annealed aluminum A1050TD with an outer diameter $D_{wp} = 40.0$ mm and a thickness of $\tau = 1.0$ mm. We assume an electrical conductivity for the workpiece of $\sigma = 36e6$ S/m. We also assume that $\epsilon = \epsilon_0$ and $\mu = \mu_0$ for workpiece and coil.

In [28] is said that $L_{cb}+L_{con}$ and $R_{cb}+R_{con}$ are less than $1.0\,\mu$H and $2.0\,$mΩ respectively. But, in [16], where it is used an EMF set-up similar to that used in [28], it is reached to the conclusion that these quantities underestimate the inductance and the resistance of the wires connecting the capacitor bank with the coil. In [16] is found that $L_{cb}+L_{con} = 2.5\,\mu$H and $R_{cb}+R_{con} = 15.0\,$mΩ are more realistic values. In this work we employ the $L_{cb} + L_{con}$ and $R_{cb} + R_{con}$ given in [16].

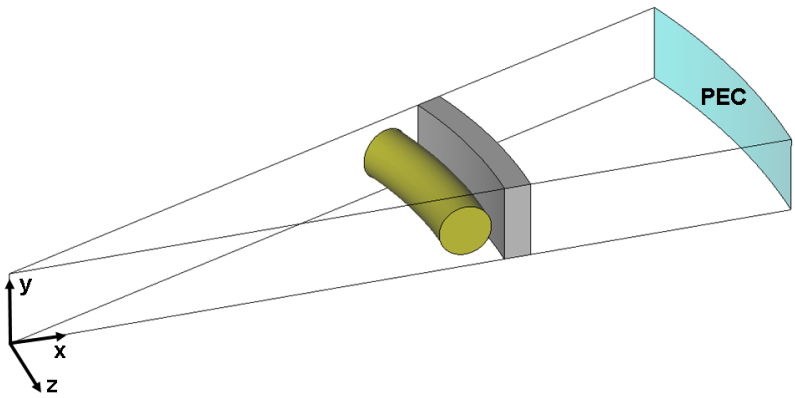

Figure 1.16: Geometry used in ERMES to compute the electromagnetic fields of the tube bulging process analyzed in [28].

1.6.2 Finite element model

The FEM model used for the tube bulging process is similar to that described in section 1.5.2. We computed the fields $\mathbf{E}(\mathbf{r},\omega)$ and $\mathbf{H}(\mathbf{r},\omega)$ in the geometry of fig. 1.16. The geometry represents a truncated portion of one turn of the coil with an angle of 20º. The problem is driven by a current density uniformly distributed in the volume of the wire. We applied the PEC boundary condition (1.22) in the colored surface of fig. 1.16. We imposed the change of coordinates explained in section 1.5.2 at each node of the FEM mesh. One of the advantages of using the geometry of fig. 1.16 is that we can obtain L_{wp} and R_{wp} for any coil length. We only need to multiply the integrals (1.1) and (1.2) performed in the volume of fig. 1.16 by $N \cdot (360^{\text{o}}/20^{\text{o}})$, where N is the number of turns of the coil.

1.6.3 Intensity through the RLC circuit

We follow the steps given in section 1.5.3 to compute the intensity flowing trough the coil of length $\ell = 200\,\text{mm}$ ($N = 68$ turns) when the capacitance is $C_{cb} = 160\,\mu$F and the initial charging energy is $U_0 = 2\,\text{kJ}$. We found that $\nu_0 = 4.6\,\text{kHz}$, $V_0 = 5\,\text{kV}$, $L_0 = 6.9\,\mu\text{H}$ and $R_0 = 101.1\,\text{m}\Omega$, being $L_0 = L_{cb} + L_{con} + L_{cw}$ and $R_0 = R_{cb} + R_{con} + R_{cw}$.

In [28] is measured the maximum current intensity for several coil lengths and capacitances C_{cb} when the initial charging energy is $U_0 = 1\,\text{kJ}$. In fig. 1.17 we compare these measurements with the results of this work.

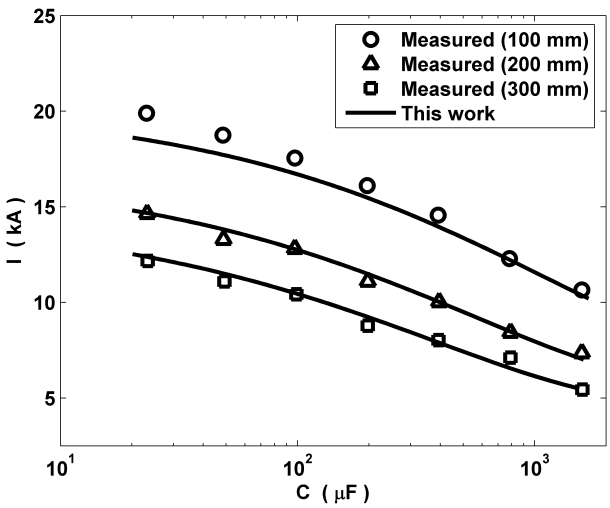

Figure 1.17: Maximum current intensity for several coil lengths and capacitances C_{cb}. The initial charging energy is $U_0 = 1\,\text{kJ}$ in all the cases. The measurements from [28] are compared with the results of this work.

1.6.4 Magnetic pressure on the workpiece

In fig. 1.18 we show the modulus of the magnetic fields $|\mathbf{H}_n(\mathbf{r}_0, \omega_0)\, I(\omega)|$, $|\mathbf{H}_n(\mathbf{r}_0, \omega)\, I(\omega)|$ and $|\mathbf{H}_n(\mathbf{r}_\tau, \omega)\, I(\omega)|$ as a function of the frequency ν, where the notation used here is the same as in section 1.5.4. In this case we can not apply the approximations (1.27) and (1.28) and we must employ the equations (1.18) and (1.17) to calculate the magnetic pressure acting on the workpiece.

In fig. 1.19 we show the magnetic pressure calculated in this work compared with the magnetic pressure calculated in [28]. We had to average the magnetic pressure over the surfaces of the workpiece to compare our results with those provided by [28].

The differences shown in fig. 1.19 can be attributed to the features of each electromagnetic model. In [28] is considered the movement of the workpiece, assumed a uniform current density along all the the length of the coil and an exponential decay of the magnetic field from the inner surface to the outer surface of the metallic tube. On the other hand, we neglected the workpiece deformation, considered a more realistic coil geometry and calculated numerically the magnetic field on the surfaces of the metallic tube.

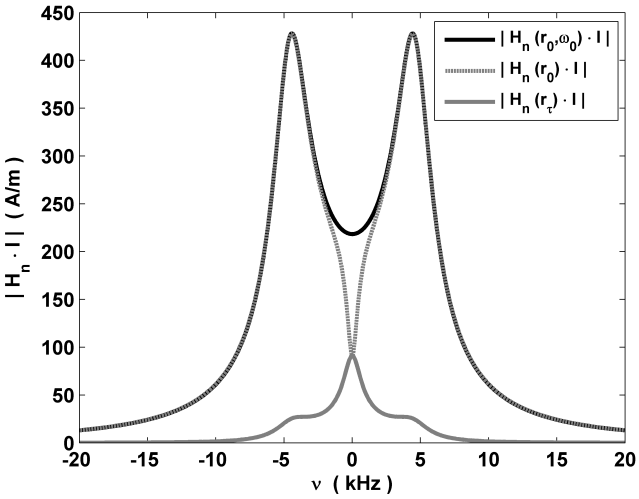

Figure 1.18: Modulus of the magnetic fields $|\mathbf{H}_n(\mathbf{r}_0, \omega_0)\, I(\omega)|$, $|\mathbf{H}_n(\mathbf{r}_0, \omega)\, I(\omega)|$ and $|\mathbf{H}_n(\mathbf{r}_\tau, \omega)\, I(\omega)|$ as a function of the frequency ν.

1.6.5 Deflection of the workpiece

We calculated the expansion of the workpiece using the mechanical model explained in section 1.5.5. The material properties and constant parameters are the same as in section 1.5.5 except for the damping coefficient α, which now is $\alpha = 693.1$.

The parameters of the mechanical model were obtained by introducing in STAMPACK the magnetic pressure calculated in [28]. Then, we adjusted the parameters until reproduce the forming velocity given in [28].

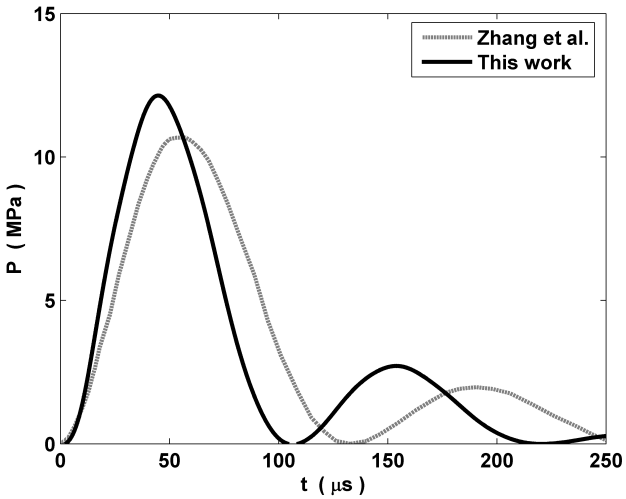

Figure 1.19: Magnetic pressure calculated by Zhang et al. [28] compared with the magnetic pressure calculated in this work.

In fig. 1.20 we compare the deflection of the workpiece deduced from [28] with the deflection of the workpiece calculated in this work. In [28] is not provided the deflection of the workpiece, we obtained it by integrating in time the forming velocity facilitated there.

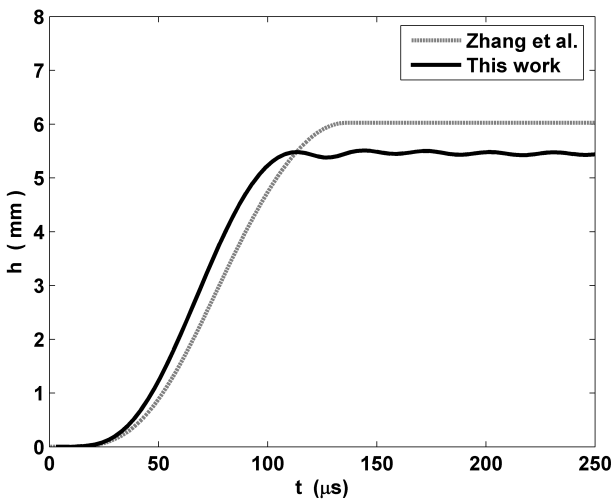

Figure 1.20: Deflection of the workpiece as a function of time. The results of Zhang et al. [28] are compared with the results of this work.

1.7 Optimum frequency and optimum capacitance

The frequency at which the discharge current oscillates is a key parameter in the design of an electromagnetic forming system. In [9, 28, 10] it is shown that, for a fixed energy U_0 and a given set of capacitor bank, connectors, coil and workpiece, there exist a frequency ν_{op} at which the maximum deformation of the workpiece is achieved. The use of this optimum frequency saves energy and prevents the premature wearing of the coil.

The frequency of the discharge ν is controlled by the capacitance C_{cb} for a given set of capacitor bank, connectors, coil and workpiece. The relationship between C_{cb} and ν is described by equations (1.7) and (1.10). Therefore, the search for the optimum frequency ν_{op} is equivalent to the search for the optimum capacitance C_{op}. Usually, in EMF, there is only a discrete set of capacitances C_{cb} available in the capacitor bank. Then, once we have determined C_{op} we must search for the closest available C_{cb}. In this work, we will refer indistinctly to the available value or to the theoretical value as the optimum capacitance C_{op}.

The optimum capacitance can be obtained computing the deformation of the workpiece for the available C_{cb} using the same initial charging energy U_0 in all the numerical simulations. Thereafter, we select the capacitance C_{cb} which produces the maximum deformation. This is the approach followed in [9, 28, 10]. We can reduce the number of electro-mechanical simulations if we make an initial estimation C_{ig} close to the optimum value C_{op}. In fact, if C_{ig} is close enough, we can find C_{op} with only three simulations. For instance, suppose that C_{ig} falls between two available capacitances C_1 and C_2, being $C_1 < C_2$. We make two electro-mechanical simulations and obtain that the deflections of the workpiece satisfy $h_1 < h_2$. Afterwards, we take a capacitance C_3 which is the lower value available such as $C_2 < C_3$. If we compute that $h_2 > h_3$ then C_2 is the optimum capacitance. In this case, we have required only three electro-mechanical simulations. On the other hand, if $h_2 < h_3$, we must keep on testing with successive C_n until find a n such as $h_n > h_{n+1}$. When this happens, we have that C_n is the optimum capacitance and $n + 1$ the number of electro-mechanical simulations. Therefore, the better C_{ig} is the less $n + 1$ is.

The simplest way to find an initial guess is derived from expression (1.25). As it is mentioned in section 1.5.3, we have observed in the literature that the typical frequencies employed in EMF lay in the interval (1.25). Therefore, we can consider an initial estimation ν_{ig} as the frequency which satisfies $\delta = \tau$.

We can improve the initial guess if we have prior knowledge about the workpiece. For instance, in [9], it is stated that the optimum frequency for the compression of a tube of thickness $\tau = 2\,\text{mm}$ made of aluminium AA3003 satisfies $\delta = 0.66\,\tau$. If we are going to use the same workpiece in a different EMF process (different coil or capacitor bank) we can try the frequency which satisfy $\delta = 0.66\,\tau$ as the initial guess. The same can be applied to the workpiece used in [28], where it is found that the optimum frequency for the expansion of a tube of thickness $\tau = 1\,\text{mm}$ made of aluminium A1050TD satisfies $\delta = 0.9\,\tau$.

In the case we do not posses any prior knowledge about workpiece we propose a method to find ν_{ig}. The idea is to look for the frequency which produces the maximum momentum $\mathbf{P}$ in the first n semi-periods, where a semi-period is half a period $T/2 = 1/2\nu$. That is, we look for the

frequency which makes maximum the quantity

$$\Delta \mathbf{P}_n = \int_0^{\frac{n}{2\nu}} \mathbf{F}_{tot} \cdot dt, \tag{1.30}$$

where $\mathbf{F}_{tot}$ is the total magnetic force acting on the workpiece and $\Delta \mathbf{P}_n$ is the momentum produced by this force in the first n semi-periods. The number n depends on the application and we obtained the best results with the minimum natural number which accomplish

$$n \geq \frac{4L_0\nu_\infty}{R_0}, \tag{1.31}$$

where L_0 and R_0 are the inductance and the resistance defined in section 1.3.3 and ν_∞ is the frequency which makes maximum the quantity $\Delta \mathbf{P}_\infty$. The quantity $\Delta \mathbf{P}_\infty$ is obtained when $n \to \infty$ in (1.30). L_0 and R_0 are evaluated at the frequency ν_∞. The expression (1.31) comes from reordering $(n/2\nu) \geq (1/\gamma_0)$, where γ_0 is defined in (1.8), and it represents the minimum number of semi-periods required to release more than 80% of the total momentum $\Delta \mathbf{P}_\infty$.

In summary, we first locate the frequency ν_∞ which makes maximum the quantity $\Delta \mathbf{P}_\infty$. Second, we compute n with (1.31) at ν_∞. Finally, ν_{ig} is the frequency which makes maximum $\Delta \mathbf{P}_n$, being n the natural number calculated in the second step. All this process is performed neglecting the workpiece deformation. We do not require any additional simulation. We are using the data obtained in the initial frequency sweep of our electromagnetic model. It takes only a few seconds to compute all the integrals and obtain ν_{ig}. In the next section we apply this method to two particular examples.

1.8 Optimum capacitance estimation

In this section we are going to obtain an initial guess C_{ig} for the tube bulging process analyzed in [28] and for the tube compression process analyzed in [9]. We apply the method proposed in section 1.7 to calculate C_{ig}.

1.8.1 Tube bulging

In [28] is analyzed the expansion of a tube by a solenoidal coil under different working conditions. They used several coils with lengths $\ell = \{100, 200, 300, 400, 500\}$ mm. They computed for each coil the bulge height with the capacitance varying from $C_{cb} = 20\,\mu$F to $C_{cb} = 1600\,\mu$F. They obtained the optimum capacitance C_{op} for each coil length and concluded that the optimum frequency satisfy $\delta = 0.9\,\tau$ in all the cases.

We analyzed this problem with the geometry, material properties and FEM model detailed in section 1.6. We found that the number defined in (1.31) is $n = 2$ in all the cases. Then, the initial guess C_{ig} is the capacitance which makes maximum the quantity $\Delta \mathbf{P}_2$ defined in (1.30). In fig. 1.21 we show the momentum $\Delta \mathbf{P}_2$ as a function of the capacitance C_{cb} for the coil lengths $\ell = \{200, 300, 400, 500\}$ mm and the initial charging energy $U_0 = 2$ kJ. In Table 1.1 we show the values of C_{ig} compared with the optimum capacitances C_{op} calculated in [28].

In [28] is also analyzed a coil with $\ell = 100\,\text{mm}$ and $U_0 = 1\,\text{kJ}$. They measure the bulge height for the capacitances $C_{cb} = \{24,$ 50, 100, 200, 400, 800, $1600\}\,\mu$F and they found that the maximum height was in $C_{cb} = 200\,\mu$F. They also calculated numerically the optimum capacitance and they obtained a value of $C_{op} = 310\,\mu$F. We calculated the initial guess with the method of section 1.7 and we found that $C_{ig} = 296\,\mu$F.

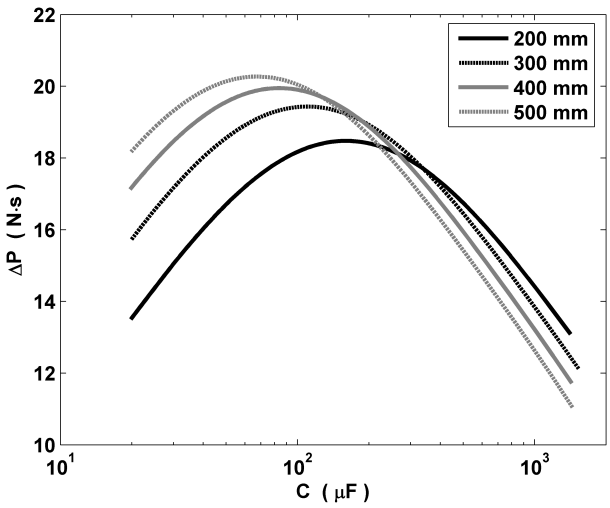

Figure 1.21: Momentum $\Delta\mathbf{P}_2$ as a function of the capacitance C_{cb} for several coil lengths. The initial charging energy is $U_0 = 2\,\text{kJ}$ in all the cases. The initial guess C_{ig} is the capacitance which makes maximum the quantity $\Delta\mathbf{P}_2$. The values of C_{ig} are shown in Table 1.1.

ℓ (mm)	C_{op} (μF)	C_{ig} (μF)
200	160	161
300	100	108
400	70	83
500	40	67

Table 1.1: Optimum capacitance (C_{op}) and initial guess (C_{ig}) for different coil lengths (ℓ).

1.8.2 Tube compression

In [9] is analyzed the compression of a tube by a solenoidal coil for the capacitances $C_{cb} = \{60,$ 120, 240, 360, 480, 600, 702, 720, 840, 960, 1080, $1800\}\,\mu$F and the initial charging energy $U_0 = 2.02\,\text{kJ}$. They computed the radial displacement of the walls of the tube and they found that the maximum displacement occurs when $C_{op} = 840\,\mu$F, $\nu_{op} = 4.97\,\text{kHz}$ and $\delta = 0.66\,\tau$.

We analyzed numerically this problem with the geometry of fig. 1.22. The geometry represents half of the coil and the workpiece placed inside a truncated portion of a semi-sphere with an angle of 20°. The FEM model used here is similar to that described in sections 1.5.2 and 1.6.2.

The workpiece is made of the aluminium alloy AA3003. The electrical conductivity is $\sigma = 29.4e6$ S/m. The outer diameter of the workpiece is $D_{wp} = 50.0$ mm. Its thickness is $\tau = 2$ mm and its length is $\ell = 100.0$ mm.

The solenoidal coil is approximated by coaxial loop currents, concentric with the workpiece and placed outside it. The coil is made of copper with a conductivity of $\sigma = 58e6$ S/m. The inner diameter of the coil is $D_c = 56.0$ mm. The separation between each loop is $p = 6.25$ mm. The length of the coil is $\ell = 100$ mm and the number of turns is $N = 17$. The dimensions of the coil wires are not provided in [9]. We assumed a thickness of $\triangle x_c = 5$ mm and a height of $\triangle y_c = 3$ mm for each coil wire.

In [9] is assumed that $R_0 = R_{cb} + R_{con} + R_{cw} = 13.03\,\mathrm{m}\Omega$ and $L_0 = L_{cb} + L_{con} + L_{cw} = 1.22\,\mu$H for all the frequencies. Therefore, for comparison purposes, we assumed the same.

We found that the maximum of $\mathbf{\Delta P}_\infty$ was in $\nu_\infty = 13$ kHz. If we substitute ν_∞, L_0 and R_0 in (1.31), we have that $n = 5$. Then, C_{ig} is the capacitance which makes maximum the quantity $\mathbf{\Delta P}_5$. In fig. 1.23 we show the momentum $\mathbf{\Delta P}_5$ as a function of the capacitance C_{cb}. The maximum is at $C_{ig} = 805\,\mu$F, $\nu_{ig} = 5$ kHz and $\delta = 0.66\,\tau$.

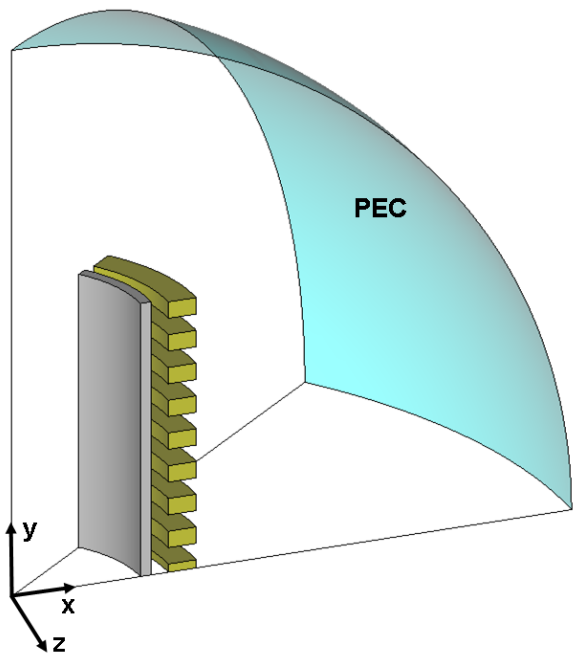

Figure 1.22: Geometry used in ERMES to compute the electromagnetic fields of the tube compression process analyzed in [9].

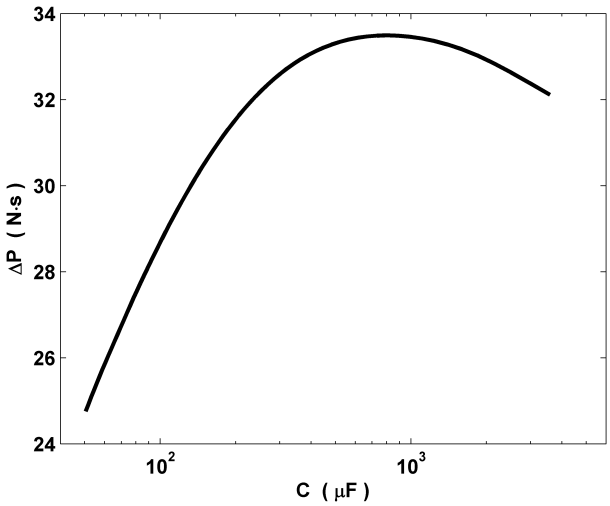

Figure 1.23: Momentum $\Delta\mathbf{P}_5$ as a function of the capacitance C_{cb}. The initial guess C_{ig} is the capacitance which makes maximum the quantity $\Delta\mathbf{P}_5$. The value of the initial guess is $C_{ig} = 805\,\mu$F.

1.9 Summary

In this report we have presented a numerical model for the simulation of electromagnetic forming processes. This method is computationally efficient because it only requires to solve the time-harmonic Maxwell equations for a few frequencies to have completely characterized the EMF system. The approach can be very useful for estimating the order of magnitude of the parameters of an EMF process, for experimentation on modeling conditions or for modeling complex geometries. Moreover, it can be easily included in a sequential coupling strategy without the worry of numerical instabilities. The method provides an explicit relation between the capacitance of the capacitor bank and the frequency of the discharge. This allow us to estimate the optimum frequency and capacitance at which it is attained the maximum workpiece deformation for a given initial energy and a given set of coil and workpiece. Also, it offers an alternative to the more extended time domain methods and a new insight into the physics of EMF. Finally, we have shown that the numerical results provided by this method exhibit a good correlation with the measurements and with the theoretical developments of other authors.

Bibliography

[1] G. Bartels, W. Schaetzing, H.-P. Scheibe, and M. Leone. Simulation models of the electromagnetic forming process. *Acta Physica Polonica A*, 115:1128–1129, 2009.

[2] W. E. Boyse, D. R. Lynch, K. D. Paulsen, and G. N. Minerbo. Nodal-based finite-element modeling of Maxwell's equations. *IEEE Transactions on Antennas and Propagation*, 40:642–651, 1992.

[3] P. Cendoya, E. Oñate, and J. Miquel. Nuevos elementos finitos para el análisis dinámico elastoplástico no lineal de estructuras laminares. Technical report, International Center for Numerical Methods in Engineering (CIMNE), ref.: M-36, 1997.

[4] M. S. Dehra. *High Velocity Formability And Factors Affecting It*. PhD thesis, The Ohio State University, 2006.

[5] A. El-Azab, M. Garnich, and A. Kapoor. Modeling of the electromagnetic forming of sheet metals: state-of-the-art and future needs. *Journal of Materials Processing Technology*, 142:744–754, 2003.

[6] FEMM. Finite element method magnetics. *David Meeker, USA. [Online]. Available: http://www.femm.info/wiki/HomePage*, 2010.

[7] G. K. Fenton and G. S. Daehn. Modelling of the electromagnetically formed sheet metal. *Journal of Materials Processing Technology*, 75:6–16, 1998.

[8] F. W. Grover. *Inductance Calculations*. Dover Publications, 2004.

[9] Y. U. Haiping and L. I. Chunfeng. Effects of current frequency on electromagnetic tube compression. *Journal of Materials Processing Technology*, 209:1053–1059, 2009.

[10] J. Jablonski and R. Winkler. Analysis of the electromagnetic forming process. *International Journal of Mechanical Sciences*, 20:315–325, 1978.

[11] J. D. Jackson. *Classical Electrodynamics*. John Wiley & Sons, Inc., 3rd edition, 1999.

[12] M. Kleiner, A. Brosius, H. Blum, F.-T. Suttmeier, M. Stiemer, B. Svendsen, J. Unger, and S. Reese. Benchmark simulation for coupled electromagnetic-mechanical metal forming processes. *Production Engineering and Development*, 11:85–90, 2004.

[13] A. G. Mamalis, D. E. Manolakos, A. G. Kladas, and A. K. Koumoutsos. Physical principles of electromagnetic forming process: a constitutive finite element model. *Journal of Materials Processing Technology*, 161:294–299, 2005.

[14] A. G. Mamalis, D. E. Manolakos, A. G. Kladas, and A. K. Koumoutsos. Electromagnetic forming tools and processing conditions: numerical simulation. *Materials and Manufacturing Processes*, 21:411–423, 2006.

[15] T. E. Manea, M. D. Verweij, and H. Blok. The importance of the velocity term in the electromagnetic forming process. *The 27th General Assembly of the International Union of Radio Science (URSI 2002), Maastricht, The Netherlands, 17-24 August*, 2002.

[16] T. E. Motoasca. *Electrodynamics in Deformable Solids for Electromagnetic Forming*. PhD thesis, Delft University of Technology, 2003.

[17] D.A. Oliveira, M.J. Worswick, M. Finn, and D. Newmanc. Electromagnetic forming of aluminum alloy sheet: Free-form and cavity fill experiments and model. *Journal of Materials Processing Technology*, 170:350–362, 2005.

[18] R. Otin. Regularized Maxwell equations and nodal finite elements for electromagnetic field computations. *Electromagnetics*, 30:190–204, 2010.

[19] J. Shang. *Electromagnetically Assisted Sheet Metal Stamping*. PhD thesis, The Ohio State University, 2006.

[20] M. A. Siddiqui. *Numerical Modelling And Simulation Of Electromagnetic Forming Process*. PhD thesis, University of Strasbourg, 2009.

[21] M. A. Siddiqui, J. P. M. Correia, S. Ahzi, and S. Belouettar. A numerical model to simulate electromagnetic sheet metal forming process. *International Journal of Material Forming*, 1:1387–1390, 2008.

[22] STAMPACK. A general finite element system for sheet stamping and forming problems. *Quantech ATZ, Barcelona, Spain. [Online]. Available: http://www.quantech.es*, 2010.

[23] J. A. Stratton. *Electromagnetic Theory*. McGraw-Hill, 1941.

[24] B. Svendsen and T. Chanda. Continuum thermodynamic formulation of models for electromagnetic thermoinelastic solids with application in electromagnetic metal forming. *Continuum Mechanics and Thermodynamics*, 17:1–16, 2005.

[25] N. Takatsu, M. Kato, K. Sato, and T. Tobe. High-speed forming of metal sheets by electromagnetic force. *The Japan Society of Mechanical Engineers International Journal*, 31:142–148, 1988.

[26] I. Ulacia, I. Hurtado, J. Imbert, M. J. Worswick, and P. L'Eplattenier. Influence of the coupling strategy in the numerical simulation of electromagnetic sheet metal forming. *The 10th International LS-DYNA Users Conference, Dearborn, Michigan USA, June 8-10*, 2008.

[27] J. Unger, M. Stiemer, M. Schwarze, B. Svendsen, H. Blum, and S. Reese. Strategies for 3D simulation of electromagnetic forming processes. *Journal of Materials Processing Technology*, 199:341–362, 2008.

[28] H. Zhang, M. Murata, and H. Suzuki. Effects of various working conditions on tube bulging by electromagnetic forming. *Journal of Materials Processing Technology*, 48:113–121, 1995.